

Comparison study of multi-slot designs in epsilon-near-zero waveguide-based electro-optical modulators

Yanhua Sha,¹ Jiaye Wu,¹ Ze Tao Xie,¹ H. Y. Fu,² and Qian Li¹

¹School of Electronic and Computer Engineering, Peking University, Shenzhen 518055, China

²Tsinghua Shenzhen International Graduate School, Tsinghua University, Shenzhen 518055, China

This work is supported by Shenzhen Science and Technology Innovation Commission (Grant No. GJHZ2018411185015272), Guangdong Basic and Applied Basic Research Foundation (Grant Nos. 2021A1515012176, 2021A1515011450), and the Youth Science and Technology Innovation Talent of Guangdong Province (Grant No. 2019TQ05X227). Corresponding author: Qian Li (e-mail: liqian@pkusz.edu.cn).

Abstract: We present a systematical comparative research on the modulation performance and the optimization of the multi-slot waveguide modulator at the telecom wavelength of 1.55 μm . It is found that the existence of epsilon-near-zero indium tin oxide slots in modulators can enhance the optical confinement, thus yielding a high extinction ratio (ER) and low insertion loss. Among the designed four types of slot modulators, the single-slot modulator exhibits the widest modulation bandwidth of 78.75 GHz and lowest energy consumption of 1.15 pJ/bit, while the dual-slot one shows the moderate performance. For the more-slot designs, the tri-slot has the advantages of a maximum figure of merit of ~ 106 , and the quadri-slot one has the highest ER of 1.38 dB/ μm . By integrating the multi-slot modulator on the silicon waveguide, the quadri-slot modulator waveguide exhibits broad optical bandwidth of 83 nm from 1479 to 1560 nm and large modulation depth (~ 18.3 dB). The performance of four types of slot modulators can be further improved from different aspects by the optimization of their geometric parameters. The results of this work could be useful in the design and selection of high performance on-chip modulators for optical communications and ultrafast data processing.

Index Terms: ENZ material, modulator, optoelectronic materials, waveguides

1. Introduction

Electro-optical modulators are the key drivers for optical communication and signal processing in short-reach interconnects in photonic integrated circuits on silicon [1], which demands higher modulation efficiency, broad optical bandwidth, small device footprint, low power consumption, and CMOS-compatibility [2], [3].

Significant development has been carried out in the conventional Si-based modulators with plasma dispersion effect where the free carrier concentration induces a change in the refractive index and absorption coefficient over a wide range of wavelengths [1]. The behaviors result in a carrier concentration change which includes carrier injection [4], depletion [5], and accumulation [6] in the p-n/p-i-n junction. For most devices based on these three mechanisms, the challenge is to maintain the modulation area efficiency without compromising operation speed in excess of gigahertz [1]. To achieve a more compact Si-based modulator, micro-ring resonator has already been introduced into waveguide-based modulator, which offers a far smaller footprint and higher modulation speed than previous Mach-Zehnder modulator [7], [8]. However, ring resonator-based modulator often suffers from fabrication tolerance constraint owing to relatively narrow optical bandwidth [1].

On the other hand, modulators also face the challenges in materials. Attempts to exploit other alternative materials, such as graphene [9], InAs [10], and transparent conducting oxides (TCOs) [11] have been proposed, and show a high modulation performance in the silicon on insulator (SOI) platform. However, graphene and InAs have disadvantages of narrow wavelength range and low carrier density, respectively, limiting their applications in modulators. TCOs have the ability to adjust carrier density from 10^{19} cm $^{-3}$ to 10^{21} cm $^{-3}$, exhibiting metallic characteristics from near-infrared to mid-infrared [12], [13]. Candidate TCOs materials such as indium tin oxide (ITO) [14], [15] and aluminum-doped zinc oxide (AZO) [16] have been investigated both numerically and experimentally in modulator application.

By adjusting the free carrier concentration, the real part of ITO's permittivity can reach a close-to-zero value at the telecommunication wavelength. This effect is so-called epsilon-near-zero (ENZ) effect, which has exhibited many fantastic optical properties, such as enhancing light-material interaction, large nonlinear responses and strong coupling phenomena, etc [17]–[20]. In addition, ITO has a slight change in carrier density and mobility in the on-chip operating temperature range, which support the modulator maintains a stable working performance [21]–[23]. Until now, a variety of ITO-based modulators have been proposed or demonstrated including hybrid modulators [24], [25] and silicon-based modulators [3], [26], [27]. Among the reported ITO-related researches, modulators featuring gigahertz-speed operation [3], ultracompact nanoscale footprint [27], and high modulation depth [28] have been verified experimentally. For electro-absorption ITO ENZ modulators based on SOI platform, silicon rib waveguide [26] and slot waveguide [29], [30] are the two most studied structures. Compared with silicon-rib waveguide modulator, which suffers from high energy-per-bit consumption, slot

waveguide modulators are capable of yielding higher modulation efficiency with lower energy consumption [29].

In recent years, slot waveguide modulators have been proven to enhance optical confinement with ultra-compactness [16], [31]. These structures mainly consist of high-index material and low-index material, thus making a large fraction of optical mode confined in the narrow slot region by utilizing electric-field discontinuity [30]. Combining with strong absorption, slot waveguide modulators can feature a high modulation efficiency. On the other hand, the performance of slot electric-optical modulator can be further improved by sandwiching a thin ENZ film waveguide, yielding a small footprint, low insertion loss and ultrahigh modulation speed [16]. Apart from amplitude modulation, the phase-shift-based ITO ENZ on-chip optical modulation applications have been investigated [32], [33].

Most of the reported slot modulators are based on the metal-oxide-semiconductor (MOS). It is demonstrated that the ENZ-based modulator with a single ITO slot possesses a higher modulation depth than one without slot [30]. A kind of plasmonic single-slot waveguide modulator consists of ITO/Al₂O₃/Au MOS structure has been experimentally studied [28]. By electrically adjusting the carrier concentration of the ITO slot, a large change of complex permittivity occurs, induces high capability of light confinement, and achieves a high modulation range of 2.71 dB/μm. But the modulator exhibits a high insertion loss and CMOS-incompatible. In addition, Sinatkas et al. investigated an electro-optical modulator developed on the Si single-slot waveguide [29]. The results showed that the waveguide has an extinction ratio (ER) of 1.11 dB/μm and insertion loss (IL) of 0.11 dB/μm. For a dual-slot modulator, the modulation efficiency can be increased by 35% as compared to the single-slot one because of a more active ENZ layer, and exhibits an ER of 1.44 dB/μm and IL of 0.037 dB/μm [34]. However, recent researches focus on the single or dual ITO slot modulators, and the impact of changes in the number of ITO slots have not been studied systematically. In addition, the mechanism analyses, optimal number of slots, and the optimization of performances in terms of ER, IL, modulation bandwidth, and energy consumption are of great importance in ENZ multi-slot modulator designs.

In this work, we propose high-efficiency electro-optical epsilon-near-zero multi-slot waveguide modulator designs, which can be controlled by applying a voltage bias. To explore the modulation performance of the modulator with different slot numbers, we perform a comparative study on the single-, dual-, tri-, and quadri-slot modulator of the multi-slot waveguide through systematic electrical and optical analyses. In the simulations, Lumerical DEVICE Solutions is employed for calculating the two-dimensional (2D) electron concentration distribution of modulation cross-section. 2D finite-difference eigenmode (FDE) method is used to numerically analyze the modulation properties of the single-, dual-, tri-, and quadri-slot modulator. Among them, the single-slot modulator has a wide bandwidth of 78.75 GHz and low energy consumption of 1.15 pJ/bit, the dual-slot modulator has the moderate performance. And the proposed tri-slot electro-optical modulator with a high ER of 1.35 dB/μm and a low IL of 0.01 dB/μm yields a higher figure of merit of ~ 106, while the quadri-slot modulator has the highest ER of 1.38 dB/μm. Furthermore, we discuss the transmission properties of the multi-slot waveguide modulators by using three-dimensional (3D) finite-difference time-domain (FDTD) method. A taper coupler is designed for coupling the ITO slot modulator and the silicon waveguide. The results indicate that the quadri-slot modulator waveguide has a broad 10 dB optical bandwidth of 83 nm from 1470 to 1553 nm, with a maximum modulation depth of up to ~ 18.3 dB. By optimizing the key geometric parameters of the multi-slot modulator, a maximum ER of 1.84 dB/μm and figure of merit of ~ 228 can be achieved respectively by the quadri-slot modulator and tri-slot modulator, while the single-slot modulator has the widest bandwidth of 83.8 GHz and the lowest energy consumption of 1.08 pJ/bit. Our work provides a guideline on choosing different types of slot modulators for different practical applications, which is beneficial in designing high performance on-chip modulators for optical communications and data processing.

This work is structured as follows. In Section 2, the design of the proposed device and the theoretical models are introduced. Subsequently, the electrical modulation mechanism is analyzed in Section 3. The performance of multi-slot modulators is compared and optimized in Section 4. Finally, a conclusion of this work is drawn in Section 5.

2. Design of the ENZ ITO multi-slot modulators

The cross-section of the proposed four slot modulators, namely, the single-, double-, tri-slot, and quadri-slot modulator are illustrated in Fig. 1 based on the SOI platform. The main components of the slot modulator are the three successive material layers: Si, insulator hafnium dioxide (HfO₂), and ITO cladding, which together form the MOS configuration to achieve tunable carrier concentration when a voltage is applied. The ITO layer is formed by doping Sn in In₂O₃ such that the free carrier concentration is at the level of 10¹⁹ cm⁻³, which is the minimum bulk electron concentration attainable in ITO to avoid being a Mott insulator [35]. ITO can exhibit a relatively high electron density and electron mobility, which offers a sufficient electrical conductivity when external electrical source is applied [36], [37]. High-k dielectric HfO₂ is chosen to provide heavy carrier concentrations in the active accumulation layer [11]. The Si rail of waveguide modulator can be fabricated through electron beam lithography and reactive ion etching. Here, the height (*h*) and the width (*w_{Si}*) of the Si rails in the four types of slot waveguide modulators structure are fixed at 220 nm and 180 nm, to facilitate the interface with common Si-photonic waveguide [29]. The 5 nm-thick HfO₂ (*t_{ox}* = 5 nm) and 20 nm-width (*w_{ITO}* = 20 nm) ITO slot filling can be deposited on the etched silicon rails using the atomic layer deposition method. In addition, the thickness *t_{ox}* of HfO₂ layer is selected based on the requirement of high bandwidth and low energy consumption [30], and the width *w_{ITO}* of ITO slot is opted due to fabrication process. The ITO layer cladding with the total thickness of *H* = 325 nm is deposited by a sputtering process to ensure that electron density in Sn-doped In₂O₃ is maintained above/equal to the critical Mott density [36]. It should be emphasized that the above geometrical parameters are selected considering the dimension requirement and optical

confinement. The ITO cladding, which serves as degenerated semiconductor with a larger number of electrons, can be regarded as a conductor. For electrical connection, the cathode and anode metal Au are connected to the ground and a forward bias (V), as shown in Fig. 1(a).

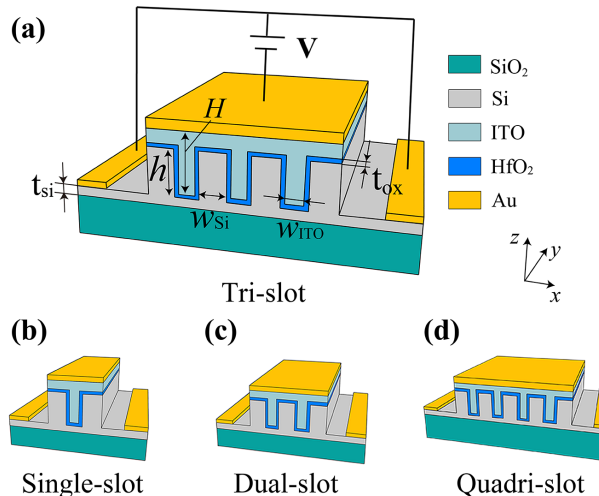


Fig. 1. Schematic diagrams of the four types of slot electric-optical modulators. (a) Tri-slot modulator. The height ($h = 220$ nm) and width of Si rails ($w_{\text{Si}} = 180$ nm), the width of ITO slot filling ($w_{\text{ITO}} = 20$ nm), the thickness of the insulator HfO_2 ($t_{\text{ox}} = 5$ nm), ITO layer cladding ($H = 325$ nm) and Si substrate ($t_{\text{Si}} = 30$ nm), are marked in the tri-slot modulator part as an example. Schematic diagrams for (b) the single-, (c) dual-, and (d) quadri-slot modulator, respectively. The four modulators have the same size and geometry parameters except for the number of slots.

The complex permittivity of ITO follows the Drude model [38], described as:

$$\epsilon = \epsilon_{\infty} - \frac{\omega_p^2}{\omega^2 - i\gamma\omega} = \epsilon_{\infty} - \frac{\omega_p^2}{\omega^2 + \gamma^2} + i \frac{\omega_p^2 \gamma}{(\omega^2 + \gamma^2)\omega}, \quad (1)$$

where the high frequency dielectric constant ϵ_{∞} is 3.9 [39], ω is the angular frequency. Plasma frequency ω_p and the collision γ are defined by:

$$\omega_p^2 = \frac{Ne^2}{e_0 m^*}, \quad (2)$$

$$\gamma = \frac{e}{\mu_n m^*}, \quad (3)$$

here, N is the free electron concentration, which ranges from 10^{19} cm^{-3} to 10^{21} cm^{-3} , determined mainly by the electric field and fabrication condition. $\mu_n = 62 \text{ cm}^2 \text{V}^{-1} \text{s}^{-1}$ is the electron mobility [30], $m^* = 0.35 m_0$ is the effective mass of electron in ITO [37]. Equation (2) shows that manipulating N will result in a change of the permittivity of ITO. The relations between the complex permittivity and the free carrier concentration of ITO at wavelength $\lambda = 1550$ nm is depicted in Fig. 2(a). By tuning the electron concentration, ϵ_{real} can approach to zero at $N_{\text{ENZ}} = 6.37 \times 10^{20} \text{ cm}^{-3}$, meaning the behavior of ITO changes from a low-loss dielectric ($\epsilon_{\text{real}} > 0$) to a high-loss metal ($\epsilon_{\text{real}} < 0$). The induced loss scales are defined as $\epsilon_{\text{imag}}/|\epsilon|^2$ [16], which reaches to the maximum value at $N_{\text{ENZ}} = 6.37 \times 10^{20} \text{ cm}^{-3}$, as shown in Fig. 2(b). The results indicate that a small change of the carrier density state near N_{ENZ} will cause a drastic change in the optical loss. Utilizing this kind of absorption mechanism, voltage-driven modulators can be designed.

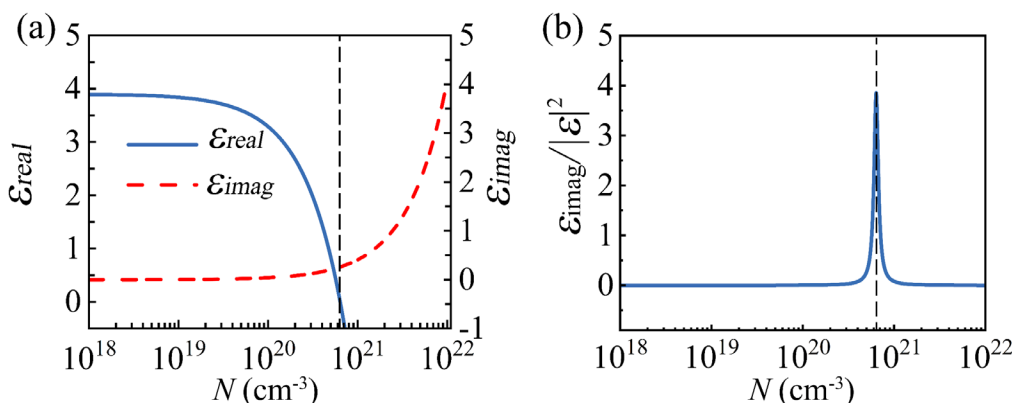


Fig.2. (a) Free electron concentration dependence of the real (ϵ_{real}) and imaginary (ϵ_{imag}) parts of the complex permittivity of ITO; (b) $\epsilon_{\text{imag}}/|\epsilon|^2$, as a function of N at the wavelength of 1550 nm. The vertical black dashed lines in (a) and (b) indicate $N_{\text{ENZ}} = 6.37 \times 10^{20} \text{ cm}^{-3}$.

3. Electrical modulation mechanism

To investigate the underlying electrical mechanism for electro-optical modulation, the electron concentration distribution of modulation cross-section under different bias modulation is studied through the commercial software Lumerical DEVICE Solutions. In this software, Poisson and drift-diffusion equations, which describe separately the electrostatic potential and density of free carriers, can be self-consistently solved. In the 2D cross-section simulation, the initial doping concentration of the ITO layer is 10^{19} cm^{-3} , and under different forward bias, electrons in ITO will redistribute. Figure 3(a) shows the equivalent one-dimensional (1D) free electron concentration distribution in the ITO-HfO₂ interface of the tri-slot modulator under the increasing forward bias, obtained by downgrading the two-dimensional (2D) cross-section. The result reveals that the free electrons tend to accumulate exponentially near the ITO-HfO₂ interface.

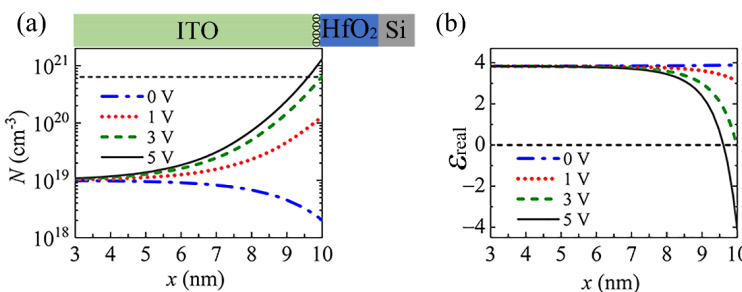


Fig.3. (a) The free electron concentration distribution in the ITO-HfO₂ interface of the tri-slot modulation part under the increasing forward bias, where N_{ENZ} occurs at the transition voltage of 3 V. The black dashed line indicates $N_{ENZ} = 6.37 \times 10^{20} \text{ cm}^{-3}$. (b) The spatial distribution of ϵ_{real} of ITO permittivity, where intersection point of the curves with the horizontal zero line reflects the position of ENZ effect.

In Fig. 3(a), the intersection of the curves and the horizontal lines show that the transition voltage occurs at approximately 3 V where the electron concentration increases to $N_{ENZ} = 6.37 \times 10^{20} \text{ cm}^{-3}$. The extremely narrow sub-nanometer accumulation layer which is related to the active ENZ effect causes the loss of the propagation mode. The carrier-induced permittivity curve at the operation wavelength of 1550 nm can be obtained through the Drude model of Eq. (1). In the ENZ-active region induced by electron accumulation layer, electric field confinement can be enhanced according to the continuity of the normalized component of electric displacement field $|E_1| = |\epsilon_2 E_2|/|\epsilon_1|$, where E_1 and E_2 are the normal components of the electric field, ϵ_1 and ϵ_2 are the complex permittivity of ITO and HfO₂, respectively. When the voltage applied to the Si increases, the induced carrier accumulation layer accompanied with the ENZ effect generates a strong confinement of the electric field. The absorption ability will be greatly enhanced at the ENZ point, where electric field E_1 grows its maximum value and $\epsilon_{imag}/|\epsilon|^2$ reaches its maximum value at the same time [16]. Figure 3(b) shows the ENZ effect achieved for every biasing value beyond the voltage threshold of 3V.

The cross-section carrier distribution results of four kinds of slot modulators are then imported into Lumerical MODE Solutions, to perform modulation property analyses.

4. Comparison and optimization of multi-slot modulators

Based on the mechanisms mentioned above, the carrier redistribution in modulator causes a change in the effective index of the guided mode and the mode loss of the whole device. In this part, 2D FDE method (Lumerical MODE Solutions) is employed to numerically analyze the modulation properties of four slot modulators.

Among the four kinds of slot modulators, different carrier distribution can generate various mode effective index (n_{eff}) to modulate optical propagation mode. For comparison, the performance evaluations of the four kinds of slot modulators are assessed in terms of their propagation loss (PL). PL is given by the mode loss equation [29]:

$$PL (\text{dB}/\mu\text{m}) = 10 \log_{10} [e^{\frac{4\pi}{\lambda} \text{Im}(n_{eff})}], \quad (4)$$

where λ is the operation wavelength and $\text{Im}(n_{eff})$ is the imaginary part of the mode effective index.

Figure 4(a) shows the variation of PL with the increase of the bias voltage. At the unbiased state (0 V), carrier accumulation is kept at a low level, and no carrier induced ENZ effect is yielded. When the voltage reached the voltage threshold of 3 V, the results are in agreement with the carrier distribution behavior predicted in Fig. 3. Specifically, PL of four slot modulators rises drastically due to ENZ effect, implying the existence of strong energy attenuation. As voltage increases to 5 V, PL remains at a stable value, owing to the unchanged thickness of the ENZ active layer. Moreover, increasing the slot number of the multi-slot modulator leads to an increment of PL. Considering the integration performance of the proposed modulator waveguide, the tri-slot modulator has a PL of 1.34 dB/ μm at 5 V, which is close to the quadri-slot, is more promising in application.

According to the response of PL to voltage, we specify 0 V as the “ON” state and 5V as the “OFF” state for the proposed multi-slot modulator waveguide. To investigate the physical mechanism of the “ON” state and the “OFF” state, we simulate respectively the electric field intensity distribution $|E_x|$ of two states and the corresponding lateral distributions for the tri-slot modulator. For the “ON” state, the electric field distribution $|E_x|$ is confined within the slot region, resides largely in the ITO slot filling, as shown in Figs. 4(b) and 4(d). In contrast, Fig. 4(c) indicates that $|E_x|$ is strongly confined in the accumulation

ITO layer at the “OFF” state. Electric field distribution $|E_x|$ in Fig. 4(e) is strongly enhanced along the slot interface under the electric displacement continuity mechanism $|E_1| = |\epsilon_2 E_2|/|\epsilon_1|$, which is more centralized than that of the “ON” state in Fig. 4(d). Therefore, PL reaches the maximum value due to the strong absorption of the ENZ ITO layer at the “OFF” state.

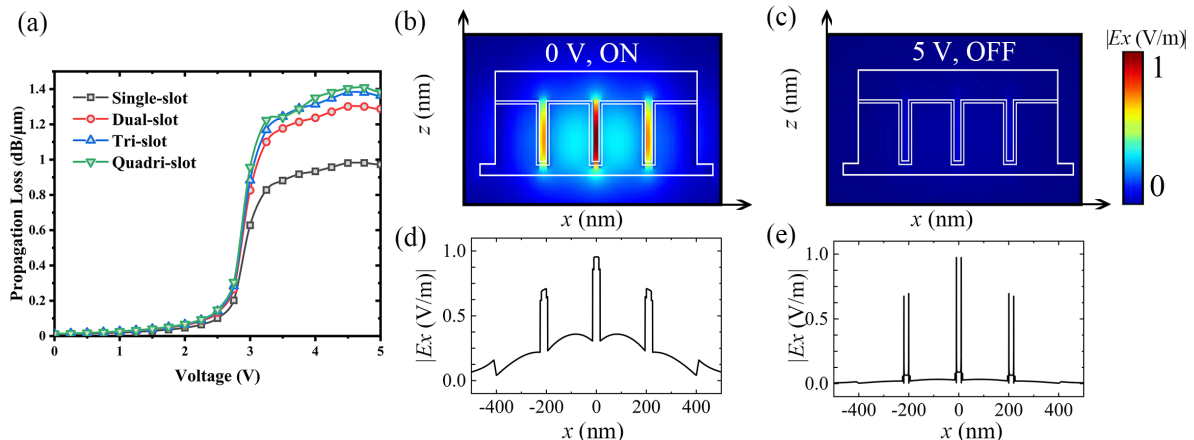


Fig. 4. (a) Propagation loss as a function of different voltage for the single-, dual-, tri-, and quadri-slot modulator. (b) and (c) are TE mode electric field intensity distribution $|E_x|$ at the “ON” and the “OFF” state, (d) and (e) are the corresponding lateral distribution of electric field at the two state for the tri-slot modulator, respectively.

To systematically study the performance of the designed electro-optical slot modulator waveguide and further optimization, the single-, dual- and quadri-slot modulators are analyzed under the identical electrical conditions and same geometric dimension except for the number of slots. Here, we also consider ER, IL and figure of merit (FoM) as important characteristics parameters for the proposed device. IL is a measure of PL at the “ON” state, while ER is the loss change of PL between the “ON” state and the “OFF” state. And FoM represents the compromise between ER and IL, which is defined by $\text{FoM} = \text{ER} / \text{IL}$ [40]. The comparison results of the performance for the four kinds of modulators are shown in Fig. 5. As can be seen in Fig. 5(a), when the slot number increases, ER raises monotonically from 0.96 to 1.38 dB/μm, and also IL raises from 0.0095 to 0.0129 dB/μm. In addition, the increment rate of the two parameters is initially fast but gradually slows down as the slot number increases. Such results happen because the increment of the overlapping active ENZ ITO areas in the slot modulator, causing a stronger the electric field confinement. And the guided mode is concentrated in the middle area of the slot modulator, while the slot far away from the center has a weaker limit absorption capacity than that of the center slot, in agreement with the electric field intensity distribution in Fig.4. Moreover, it can be observed that the tri-slot modulator gains a maximum FoM of ~ 106 with an ER of 1.35 dB/μm and an IL of 0.01 dB/μm among four types of slot modulators, as presented by the red line in Fig. 5(b).

In addition, modulation bandwidth (also known as electrical frequency response range) and energy consumption are important performance factors of optical modulators. Since the slot modulator is based on the MOS-like configuration, the bandwidth is determined typically by the RC delay from the modulator itself when no external resistance and capacitance exist. Here, we estimated the modulation bandwidth (BW) and the average energy consumption (P) using $\text{BW} = 1/(2\pi RC)$ [41] and $P = CV^2/4$ [41], where R and C are the equivalent resistance and the capacitance of the device, $V = 5$ V is the applied voltage. The resistivity of the silicon applied in the modulator is about $110 \Omega \cdot \mu\text{m}$ when the doping concentration is $3 \times 10^{18} \text{ cm}^{-3}$ [42]. And the unit area capacitance is approximated as $\epsilon_0 \epsilon_r / d$, where $\epsilon_r = 25$ is the relative dielectric constant of insulating medium HfO_2 , ϵ_0 is the dielectric constant of vacuum, and $d = 5 \text{ nm}$ is the thickness of the insulating medium HfO_2 . As an example, for the tri-slot modulator as shown in Fig. 1(a), the equivalent R and C are approximately calculated to $55 \Omega \cdot \mu\text{m}$ (parallel resistance) and $9.43 \times 10^{-14} \text{ F}/\mu\text{m}$. Therefore, the modulation bandwidth and the energy consumption are estimated as 30.7 GHz and 2.95 pJ/bit, respectively. As illustrated by the blue line in Fig. 5(b), the modulation bandwidth decreases with the increase of the number of the slot modulator, and the single-slot modulator has a broad bandwidth of 78.75 GHz among the four types of slot modulators. Such results are due to the increment of the capacitance when increasing the number of the slot modulator.

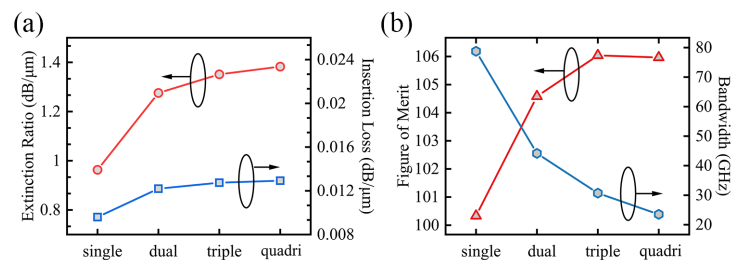


Fig. 5. (a) Extinction ratio and insertion loss, (b) figure of merit and bandwidth of the four kinds of slot modulators under the identical electrical conditions and same geometric dimension except for the number of slots.

In order to study optical transmission properties of the multi-slot modulator, the ENZ slot modulator waveguide is

demonstrated, which includes the ENZ ITO slot modulator, input and output taper coupler part, as shown in Fig. 6(a). A taper coupler of appropriate size was designed to couple the TE-mode into the 450×250 nm silicon waveguide. The length L_2 of the ENZ ITO slot modulator is set to 5.0 μm , and the internal parameters are set as described in Fig. 1. The 3D finite-difference time-domain (FDTD) method (Lumerical FDTD solutions) is used to numerically analyze the optical transmission property of the four types of the modulator waveguide. As an example, Fig. 6(b) and 6(c) display the propagation field profiles $|E_x|$ at the “ON” state and the “OFF” state modulator waveguide, where the TE-mode light source with $\lambda = 1550$ nm is launched into the waveguide. At the “ON” state, the guided mode propagates along through the waveguide without obvious absorption loss. The total PL is 0.31 dB from the input end to the output end, including IL of 0.14 dB and the coupling loss of 0.17 dB. For the tri-slot modulator, the $|E_x|$ field is mainly distributed in the middle area of the slot modulator, which consistent with the 2D mode analysis result in Fig. 4(b) and 4(d). At the “OFF” state, the guided mode is absorbed and cut off by the active modulator based on ENZ ITO effect. The total PL is 11.6 dB and ER is 11.29 dB, which corresponds to 2.26 dB/ μm at the length of 5 μm . Moreover, Fig. 6(c) indicates that $|E_x|$ has been attenuated completely after 3 μm propagation in the modulation part, and the modulator length L_2 can be reduced further to 3 μm corresponding to ER = 3.76 dB/ μm . Figure. 7 shows ER of the proposed ENZ slot modulator waveguide at different wavelengths. As can be seen, the working wavelength for the single-, dual-, tri- and quadri-slot modulator waveguide with ER exceeds 10 dB are from 1482 to 1538 nm, 1474 to 1550 nm, 1479 to 1560 nm, and 1470 to 1553 nm, respectively, with a maximum modulation depth of up to ~ 13.0 dB, ~ 16.45 dB, ~ 15.6 dB, and ~ 18.3 dB. Thus, broad optical bandwidth of 56 nm, 76 nm, 81 nm, and 83 nm, or a working frequency range 7.4 THz, 10.0 THz, 10.5 THz, 10.9 THz, can be exhibited by the single-, dual-, tri- and quadri-slot modulator waveguide with the modulator length of 5 μm .

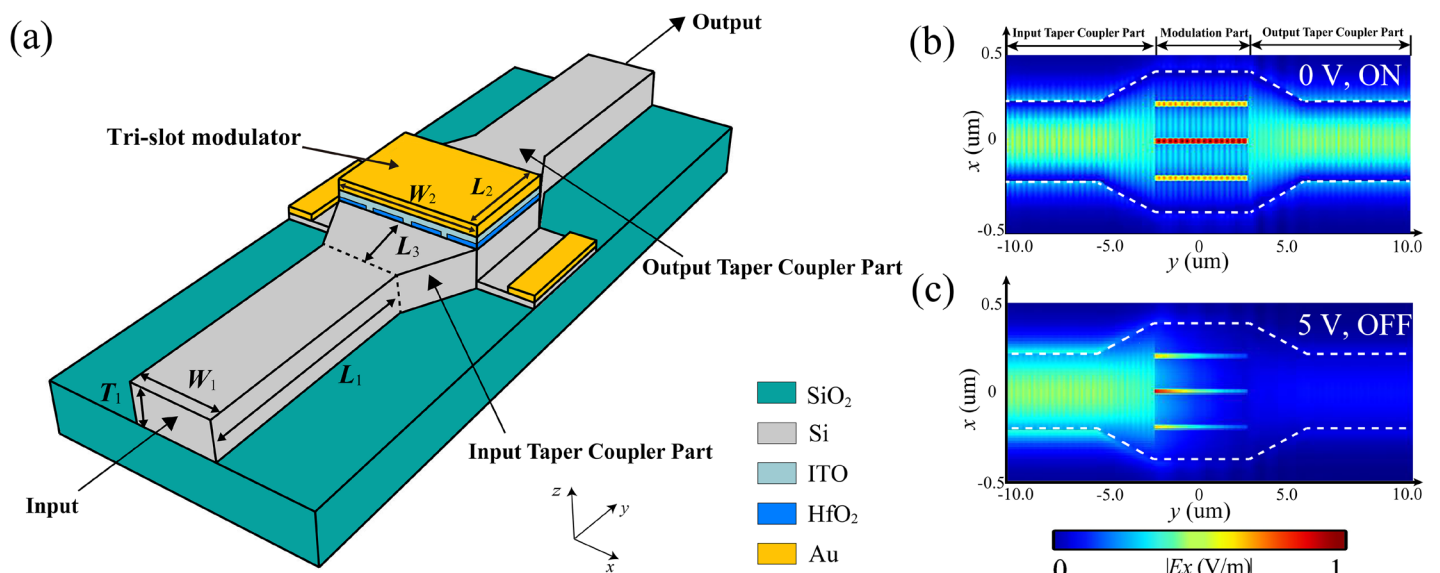


Fig. 6. (a) 3D schematic of the ENZ slot waveguide modulator (take tri-slot as an example). The thickness, width and length of the silicon waveguide is $T_1 = 250$ nm, $W_1 = 450$ nm and $L_1 = 5$ μm , respectively. W_2 and $L_2 = 5$ μm represent the width and length of the slot modulator. And the taper coupler structure has a length $L_3 = 3$ μm . Top view (x-y plane) of propagation field profiles $|E_x|$ at (b) the “ON” state and (c) the “OFF” state.

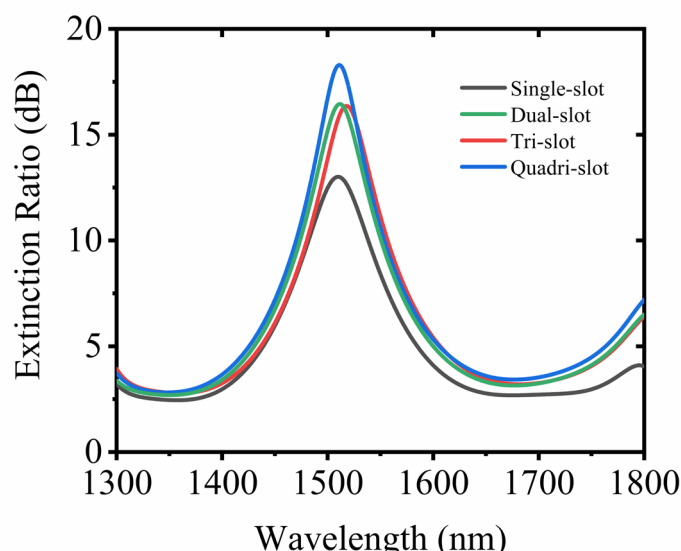


Fig. 7. Extinction ratio of the multi-slot waveguide modulator as a function of the wavelength.

As a summary, Table 1 shows a comparison of performance among the slot modulator proposed in this paper. The single-slot modulator has a wide modulation bandwidth of 78.75 GHz and low energy consumption of 1.15 pJ/bit compared with other modulators. Additionally, the tri-slot modulator has the highest FoM of \sim 106, and the quadri-slot modulator waveguide has the broadest optical bandwidth of 83 nm among four types of modulators. Based on the comparative results, four types of slot modulators can be considered for different practical applications. For example, the single-slot modulator can be used for optical communication and signal processing which requires broad bandwidth and low energy consumption, while the tri-slot modulator can be used for those needing high FoM. And the quadri-slot modulator is suitable for optical communication systems that require high bandwidth and modulation depth.

Table 1

Comparison of the modulation performance for four types of slot modulators. For ER, IL, FoM, BW and P , operating at 1.55 μ m.

Types of slot	ER (dB/ μ m)	IL (dB/ μ m)	FoM	BW (GHz)	P (pJ/bit)	Wavelength range
Single-slot	0.96	0.0095	100.33	78.15	1.15	56 nm (1482 – 1538 nm)
Dual-slot	1.28	0.0121	104.58	44.16	2.05	76 nm (1474 – 1550 nm)
Tri-slot	1.35	0.0127	106.03	30.69	2.95	81 nm (1479 – 1560 nm)
Quadri-slot	1.38	0.0129	105.96	23.51	3.85	83 nm (1470 – 1553 nm)

To further improve the performance of the multi-slot modulator, the key geometric parameters the width of ITO slot filling w_{ITO} and the width of Si rails w_{Si} are optimized in terms of ER, IL and bandwidth. Figure 8(a)–(d) shows ER, IL and bandwidth of the multi-slot modulator as a function of w_{ITO} and w_{Si} . The sweeping results of four types of slot modulators indicate that the increase of w_{Si} leads to a lower ER and IL, while the increase of w_{ITO} induces a lower ER and higher IL. When the number of slots is decreased, w_{ITO} and w_{Si} of each slot modulator all lead to lower bandwidth. For the kinds of four modulators, optimizing geometric parameters leads to drastic changes to ER compared with modulation bandwidth. As for each type of slot modulator, ER, FoM, and modulation bandwidth have maximum values when the optimal geometric parameters of $w_{ITO} = 10$ and $w_{Si} = 160$ nm. Table 2 states optimal performance of four types of slot modulators after optimizing their geometric parameters. The single-slot has the widest modulation bandwidth of 83.3 GHz and lowest energy consumption of 1.08 pJ/bit among four modulators. Besides, the performances of the dual-slot modulator have been improved after optimizing. The tri-slot modulator has the largest FoM of 228.12 and the quadri-slot modulator has the highest ER of 1.84 dB/ μ m, which increased respectively by 115% and 33% respectively compared to their unoptimized performance. Therefore, the type of the multi-slot modulator can be selected according to the requirements for practical applications.

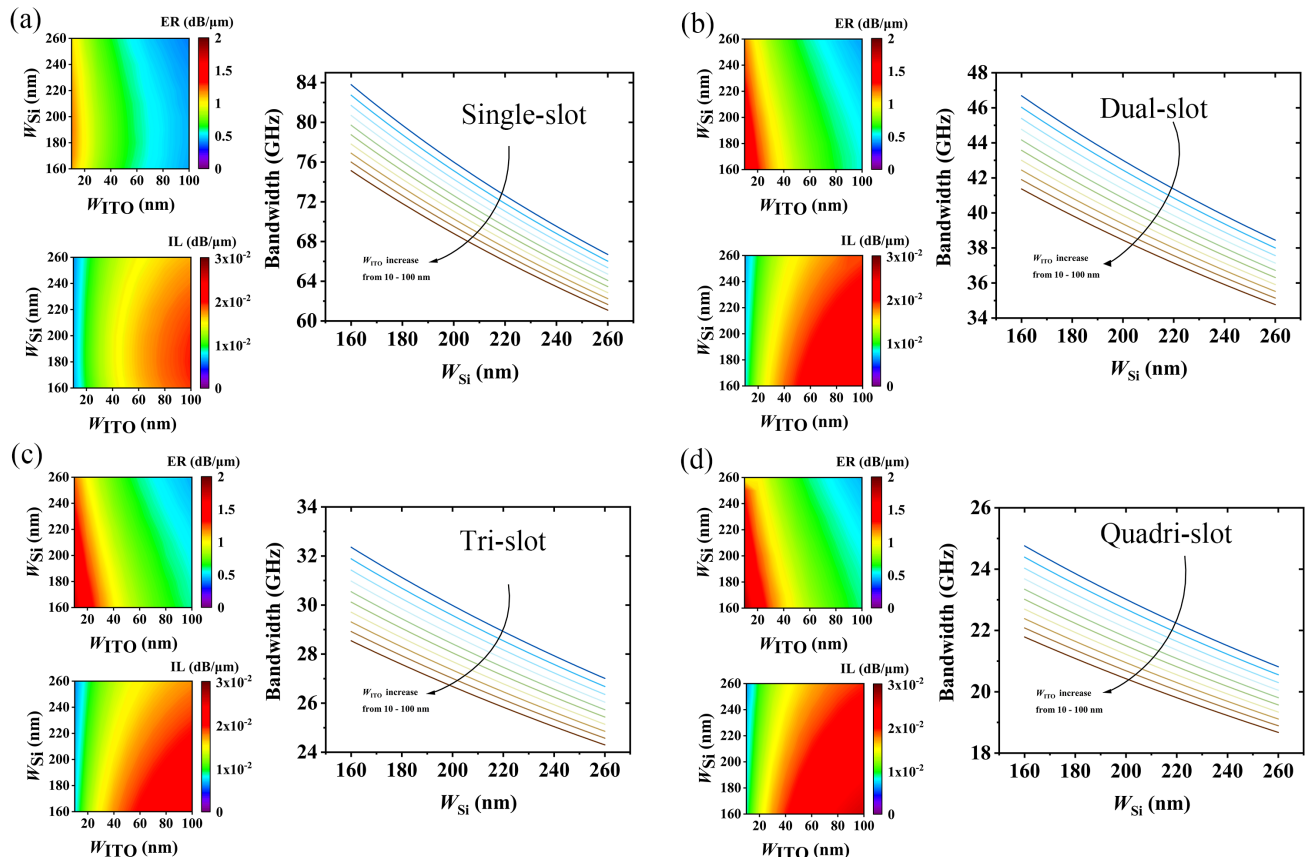


Fig. 8. Geometric parameters optimization of modulation performance including ER, IL and bandwidth for (a) single-slot modulator, (b) dual-slot modulator, (c) tri-slot modulator and (d) quadri-slot modulator.

Table 2

Analyses of the optimal modulation performance. Four types of slot modulators have the same optimized geometric parameter $w_{\text{ITO}} = 10 \text{ nm}$ and $w_{\text{Si}} = 160 \text{ nm}$.

Types of slot	ER (dB/ μm)	IL (dB/ μm)	FoM	BW (GHz)	P (pJ/bit)
Single-slot	1.14	0.0064	177.57	83.80	1.08
Dual-slot	1.64	0.0081	202.20	46.69	1.94
Tri-slot	1.77	0.0078	228.12	32.35	2.79
Quadri-slot	1.84	0.0087	212.72	24.76	3.65

5. Conclusions

In this work, the multi-slot modulators based on ENZ effect waveguide have been systematically designed and comparatively studied by electrical and optical analyses. The advantage of the slot structure and ENZ effect have been combined to achieve high modulation efficiency. In order to realize ENZ effect, the free electron concentration of ITO has been calculated. 2D mode analysis and calculated results show that the single-slot waveguide has the widest modulation bandwidth of 78.15 GHz and lowest energy consumption of 1.15 pJ/bit. The dual-slot has the moderate performance among four types modulators. And the tri-slot modulator has the maximum FoM of ~ 106 , while quadri-slot modulator yields a modulation performance of a high ER = 1.38 dB/ μm . Meanwhile, 3D optical transmission simulation demonstrates the quadri-slot modulator waveguide has a broad 10 dB optical bandwidth of 83 nm, or a 10.9 THz, with a maximum modulation depth of up to ~ 18.3 dB. Finally, the optimized results show that the broadest modulation bandwidth and the lowest energy consumption are estimated to be about 83.8 GHz and 1.08 pJ/bit for the single-slot modulator, the tri-slot modulator and quadri-slot modulator can achieve maximum FoM = ~ 228 and ER = 1.84 dB/ μm . The comparative results of our work provide a proposal for choosing different types of slot modulators based on the practical applications, and could be useful in the development of the on-chip modulators for ultrafast optical communications and signal processing.

References

- [1] G. T. Reed, G. Mashanovich, F. Y. Gardes, and D. J. Thomson, "Silicon optical modulators," *Nat. Photonics*, vol. 4, no. 8, pp. 518–526, 2010, doi: 10.1038/nphoton.2010.179.
- [2] V. J. Sorger, N. D. Lanzillotti-Kimura, R. M. Ma, and X. Zhang, "Ultra-compact silicon nanophotonic modulator with broadband response," *Nanophotonics*, vol. 1, no. 1, pp. 17–22, 2012, doi: 10.1515/nanoph-2012-0009.
- [3] M. G. Wood *et al.*, "Gigahertz speed operation of epsilon-near-zero silicon photonic modulators," *Optica*, vol. 5, no. 3, p. 233, 2018, doi: 10.1364/optica.5.000233.
- [4] F. Neumann, Y. A. Genenko, C. Melzer, S. V. Yampolskii, and H. Von Seggern, "Self-consistent analytical solution of a problem of charge-carrier injection at a conductor/insulator interface," *Phys. Rev. B - Condens. Matter Mater. Phys.*, vol. 75, no. 20, pp. 1–10, 2007, doi: 10.1103/PhysRevB.75.205322.
- [5] A. Liu *et al.*, "High-speed optical modulation based on carrier depletion in a silicon waveguide," *Opt. Express*, vol. 15, no. 2, p. 660, 2007, doi: 10.1364/oe.15.000660.
- [6] A. Liu *et al.*, "A high-speed silicon optical modulator based on a metal-oxide-semiconductor capacitor," *Nature*, vol. 427, no. 6975, pp. 615–618, 2004, doi: 10.1038/nature02310.
- [7] Q. Xu, B. Schmidt, S. Pradhan, and M. Lipson, "Micrometre-scale silicon electro-optic modulator," *Nature*, vol. 435, no. 7040, pp. 325–327, 2005, doi: 10.1038/nature03569.
- [8] E. Timurdogan, C. M. Sorace-Agaskar, J. Sun, E. Shah Hosseini, A. Biberman, and M. R. Watts, "An ultralow power athermal silicon modulator," *Nat. Commun.*, vol. 5, pp. 1–11, 2014, doi: 10.1038/ncomms5008.
- [9] H. Yan *et al.*, "Damping pathways of mid-infrared plasmons in graphene nanostructures," *Nat. Photonics*, vol. 7, no. 5, pp. 394–399, 2013, doi: 10.1038/nphoton.2013.57.
- [10] M. Wagner *et al.*, "Ultrafast dynamics of surface plasmons in InAs by time-resolved infrared nanospectroscopy," *Nano Lett.*, vol. 14, no. 8, pp. 4529–4534, 2014, doi: 10.1021/nl501558t.
- [11] V. E. Babicheva, A. Boltasseva, and A. V. Lavrinenko, "Transparent conducting oxides for electro-optical plasmonic modulators," *Nanophotonics*, vol. 4, no. 1, pp. 165–185, 2015, doi: 10.1515/nanoph-2015-0004.
- [12] Y. Zhu, X. Hu, Y. Fu, H. Yang, and Q. Gong, "Ultralow-power and ultrafast all-optical tunable plasmon-induced transparency in metamaterials at optical communication range," *Sci. Rep.*, vol. 3, no. October 2015, 2013, doi: 10.1038/srep02338.
- [13] M. Abb, Y. Wang, C. H. De Groot, and O. L. Muskens, "Hotspot-mediated ultrafast nonlinear control of multifrequency plasmonic nanoantennas," *Nat. Commun.*, vol. 5, no. June 2016, pp. 1–8, 2014, doi: 10.1038/ncomms5869.
- [14] S. Rajput, V. Kaushik, S. Jain, P. Tiwari, A. K. Srivastava, and M. Kumar, "Optical Modulation in Hybrid Waveguide Based on Si-ITO Heterojunction," *J. Light. Technol.*, vol. 38, no. 6, pp. 1365–1371, 2020, doi: 10.1109/JLT.2019.2953690.
- [15] B. Zhou, E. Li, Y. Bo, and A. X. Wang, "High-Speed Plasmonic-Silicon Modulator Driven by Epsilon-Near-zero Conductive Oxide," *J. Light. Technol.*, vol. 38, no. 13, pp. 3338–3345, 2020, doi: 10.1109/JLT.2020.2979192.
- [16] Z. Lu, W. Zhao, and K. Shi, "Ultracompact electroabsorption modulators based on tunable epsilon-near-zero-slot waveguides," *IEEE Photonics J.*, vol. 4, no. 3, pp. 735–740, 2012, doi: 10.1109/JPHOT.2012.2197742.
- [17] J. Wu, B. A. Malomed, H. Y. Fu, and Q. Li, "Self-interaction of ultrashort pulses in an epsilon-near-zero nonlinear material at the telecom wavelength," *Opt. Express*, vol. 27, no. 26, p. 37298, 2019, doi: 10.1364/oe.27.037298.

- [18] J. Wu, Z. T. Xie, Y. Sha, H. Y. Fu, and Q. Li, "Comparative study on epsilon-near-zero transparent conducting oxides: High-order chromatic dispersions and modeling of ultrashort pulse interactions," *Phys. Rev. A*, vol. 102, no. 5, pp. 1–7, 2020, doi: 10.1103/PhysRevA.102.053503.
- [19] M. Z. Alam, I. De Leon, and R. W. Boyd, "Large optical nonlinearity of indium tin oxide in its epsilon-near-zero region," *Science (80-.)*, vol. 352, no. 6287, pp. 795–797, 2016, doi: 10.1126/science.aae0330.
- [20] O. Reshef, I. De Leon, M. Z. Alam, and R. W. Boyd, "Nonlinear optical effects in epsilon-near-zero media," *Nat. Rev. Mater.*, vol. 4, no. 8, pp. 535–551, 2019, doi: 10.1038/s41578-019-0120-5.
- [21] D. H. Zhang and H. L. Ma, "Scattering mechanisms of charge carriers in transparent conducting oxide films," *Appl. Phys. A Mater. Sci. Process.*, vol. 62, no. 5, pp. 487–492, 1996, doi: 10.1007/BF01567122.
- [22] A. Ambrosini *et al.*, "Variable-temperature electrical measurements of zinc oxide/tin oxide-cosubstituted indium oxide," *Chem. Mater.*, vol. 14, no. 1, pp. 52–57, 2002, doi: 10.1021/cm0100725.
- [23] N. Taga, H. Odaka, Y. Shigesato, I. Yasui, M. Kamei, and T. E. Haynes, "Electrical properties of heteroepitaxial grown tin-doped indium oxide films," *J. Appl. Phys.*, vol. 80, no. 2, pp. 978–984, 1996, doi: 10.1063/1.362910.
- [24] M. Y. Abdelatty, "High-speed hybrid plasmonic electro-optical absorption modulator exploiting epsilon-near-zero effect in indium-tin-oxide," *J. Nanophotonics*, vol. 12, no. 03, p. 1, 2018, doi: 10.1117/1.jnp.12.036011.
- [25] M. A. Swillam, A. O. Zaki, K. Kirah, and L. A. Shahada, "On Chip Optical Modulator using Epsilon-Near-Zero Hybrid Plasmonic Platform," *Sci. Rep.*, vol. 9, no. 1, pp. 1–9, 2019, doi: 10.1038/s41598-019-42675-z.
- [26] M. Ayata, Y. Nakano, and T. Tanemura, "Silicon rib waveguide electro-absorption optical modulator using transparent conductive oxide bilayer," *Jpn. J. Appl. Phys.*, vol. 55, no. 4, 2016, doi: 10.7567/JJAP.55.042201.
- [27] E. Li, Q. Gao, R. T. Chen, and A. X. Wang, "Ultracompact Silicon-Conductive Oxide Nanocavity Modulator with 0.02 Lambda-Cubic Active Volume," *Nano Lett.*, vol. 18, no. 2, pp. 1075–1081, 2018, doi: 10.1021/acs.nanolett.7b04588.
- [28] H. W. Lee *et al.*, "Nanoscale conducting oxide PlasMOStor," *Nano Lett.*, vol. 14, no. 11, pp. 6463–6468, 2014, doi: 10.1021/nl502998z.
- [29] G. Sinatkas, A. Pitilakis, D. C. Zografopoulos, R. Beccherelli, and E. E. Kriegis, "Transparent conducting oxide electro-optic modulators on silicon platforms: A comprehensive study based on the drift-diffusion semiconductor model," *J. Appl. Phys.*, vol. 121, no. 2, 2017, doi: 10.1063/1.4973896.
- [30] X. Liu *et al.*, "Epsilon-Near-Zero Si Slot-Waveguide Modulator," *ACS Photonics*, vol. 5, no. 11, pp. 4484–4490, 2018, doi: 10.1021/acspophotonics.8b00945.
- [31] Z. Lu and W. Zhao, "Nanoscale electro-optic modulators based on graphene-slot waveguides," vol. 29, no. 6, pp. 1490–1496, 2012.
- [32] J. Baek, J.-B. You, and K. Yu, "Free-carrier electro-refraction modulation based on a silicon slot waveguide with ITO," *Opt. Express*, vol. 23, no. 12, p. 15863, 2015, doi: 10.1364/oe.23.015863.
- [33] G. Sinatkas and E. E. Kriegis, "Silicon-Photonic Electro-Optic Phase Modulators Integrating Transparent Conducting Oxides," *IEEE J. Quantum Electron.*, vol. 54, no. 4, p. 1, 2018, doi: 10.1109/JQE.2018.2852144.
- [34] Y. Kuang, "A Dual-Slot Electro-Optic Modulator Based on an Epsilon-Near-Zero Oxide A Dual-Slot Electro-Optic Modulator Based on an Epsilon-Near-Zero Oxide," vol. 11, no. 4, 2019, doi: 10.1109/JPHOT.2019.2927756.
- [35] A. P. Vasudev, J.-H. Kang, J. Park, X. Liu, and M. L. Brongersma, "Electro-optical modulation of a silicon waveguide with an 'epsilon-near-zero' material," *Opt. Express*, vol. 21, no. 22, p. 26387, 2013, doi: 10.1364/oe.21.026387.
- [36] Z. Ma, Z. Li, K. Liu, C. Ye, and V. J. Sorger, "Indium-Tin-Oxide for High-performance Electro-optic Modulation," *Nanophotonics*, vol. 4, no. 1, pp. 198–213, 2015, doi: 10.1515/nanoph-2015-0006.
- [37] P. P. Edwards, A. Porch, M. O. Jones, D. V. Morgan, and R. M. Perks, "Basic materials physics of transparent conducting oxides," *Dalt. Trans.*, no. 19, pp. 2995–3002, 2004, doi: 10.1039/b408864f.
- [38] S. A. Maier, *Plasmonics: fundamentals and applications*. Springer Science & Business Media, 2007.
- [39] F. Michelotti, L. Dominici, E. Descrovi, N. Danz, and F. Menchini, "Thickness dependence of surface plasmon polariton dispersion in transparent conducting oxide films at 155 μm," *Opt. Lett.*, vol. 34, no. 6, p. 839, 2009, doi: 10.1364/ol.34.000839.
- [40] A. Melikyan, T. Vallaitis, N. Lindenmann, T. Schimmel, W. Freude, and J. Leuthold, "A surface plasmon polariton absorption modulator," *Opt. InfoBase Conf. Pap.*, vol. 19, no. 9, pp. 8855–8869, 2010, doi: 10.1364/cleo.2010.jthe77.
- [41] X. Peng *et al.*, "Highly efficient graphene-on-gap modulator by employing the hybrid plasmonic effect," *Opt. Lett.*, vol. 42, no. 9, pp. 1736–1739, 2017.
- [42] S. Basu and B. J. Lee, "Infrared Radiative Properties of Heavily Doped Silicon at Room Temperature," vol. 132, no. February 2010, pp. 1–8, 2013, doi: 10.1115/1.4000171.